

Anisotropic exchange interaction of two hole-spin qubits

Received: 21 December 2022

Accepted: 15 March 2024

Published online: 06 May 2024

 Check for updates

Simon Geyer¹✉, Bence Hetényi^{1,2}, Stefano Bosco¹,
Leon C. Camenzind^{1,3}, Rafael S. Egli¹, Andreas Fuhrer², Daniel Loss¹,
Richard J. Warburton¹, Dominik M. Zumbühl¹✉ &
Andreas V. Kuhlmann¹✉

Semiconductor spin qubits offer the potential to employ industrial transistor technology to produce large-scale quantum computers. Silicon hole spin qubits benefit from fast all-electrical qubit control and sweet spots to counteract charge and nuclear spin noise. However, the demonstration of a two-qubit interaction has remained an open challenge. One missing factor is an understanding of the exchange coupling in the presence of a strong spin–orbit interaction. Here we study two hole-spin qubits in a silicon fin field-effect transistor, the workhorse device of today’s semiconductor industry. We demonstrate electrical tunability of the exchange splitting from above 500 MHz to close-to-off and perform a conditional spin-flip in 24 ns. The exchange is anisotropic because of the spin–orbit interaction. Upon tunnelling from one quantum dot to the other, the spin is rotated by almost 180 degrees. The exchange Hamiltonian no longer has the Heisenberg form and can be engineered such that it enables two-qubit controlled rotation gates without a trade-off between speed and fidelity. This ideal behaviour applies over a wide range of magnetic field orientations, rendering the concept robust with respect to variations from qubit to qubit, indicating that it is a suitable approach for realizing a large-scale quantum computer.

Semiconductor quantum dot (QD) spin qubits are prime candidates for future implementations of large-scale quantum circuits^{1–3}. Currently, the most advanced spin-based quantum processor allows for universal control of six electron spin qubits in silicon (Si)⁴, closely followed by a four-qubit demonstration with holes in germanium⁵. In comparison to electron spins, hole spins have the advantage that they can be controlled all-electrically, without the added complexity of on-chip micromagnets^{6,7} or the need for orbital degeneracy⁸, thanks to their intrinsic spin–orbit interaction (SOI). Moreover, holes benefit from a reduced hyperfine interaction⁹ and the absence of valleys¹⁰.

Holes in quasi-one-dimensional (1D) nanostructures are highly attractive for implementing fast and coherent qubits. The mixing of heavy- and light-hole states on account of the 1D-confinement results in an unusually strong and electrically tunable direct Rashba SOI, with

sweet spots for charge and hyperfine noise^{11–13}, enabling ultra-fast hole spin qubits^{14,15} with reduced sensitivity to noise¹⁶. Conveniently, such a 1D-system can be realized using today’s industry standard transistor design known as the fin field-effect transistor (FinFET)¹⁷. Adapting FinFETs for QD integration^{16,18–22} potentially facilitates quantum computer scale-up by leveraging decades of technology development in the semiconductor industry²³. Furthermore, recent research has shown that individual hole spin qubits in a bulk-Si FinFET can be operated at temperatures above 4 K (ref. 22), paving the way for FinFET-based quantum integrated circuits that host both the qubit array and its classical control electronics on the same chip^{24–26}.

Universal quantum computation requires both single-qubit control and two-qubit interactions. Native two-qubit gates for spins such as the $\sqrt{\text{SWAP}}$ (refs. 1,27), the controlled phase^{28–31} or the controlled

¹Department of Physics, University of Basel, Basel, Switzerland. ²IBM Research Europe-Zurich, Rüschlikon, Switzerland. ³Present address: RIKEN, Center for Emergent Matter Science (CEMS), Wako-shi, Japan. ✉ e-mail: simon.geyer@unibas.ch; dominik.zumbuhl@unibas.ch; andreas.kuhlmann@unibas.ch

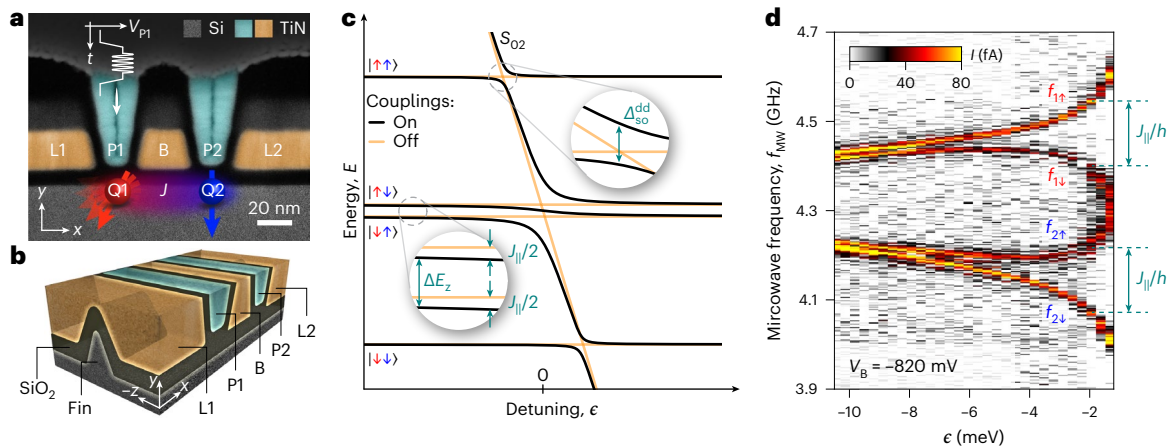


Fig. 1 | Two-qubit system in a Si FinFET. a, False-colour transmission electron microscope image of a co-fabricated device showing the cross-section along the fin. The qubits (Q1, Q2) are located underneath the plunger gates (P1, P2) and are manipulated by applying microwaves to the P1-gate. The barrier gate (B) controls the interdot tunnelling; the lead gates (L1, L2) accumulate the hole reservoirs. Measurements are performed on a device with ≈ 20 nm-wide B- and P-gates. **b**, A three-dimensional render of the device, illustrating the triangular-shaped fin covered by the wrap-around gates. **c**, Two-spin energy-level diagram close to the

(1,1)–(0,2) charge transition with (black) and without (orange) interactions. A g -tensor mismatch yields the singlet–triplet mixed states $|\uparrow\downarrow\rangle, |\downarrow\uparrow\rangle$. The singlet state S_{02} hybridizes with the antiparallel (parallel) two-spin states on account of spin-conserving tunnelling (SOI). A finite exchange splitting J_{\parallel} lowers the energy of the antiparallel two-spin states with respect to the parallel ones. **d**, Exchange spin funnel measurements for both qubits, revealing an increase (decrease) in $f_{1\uparrow}, f_{2\uparrow}, f_{1\downarrow}, f_{2\downarrow}$ at the upper (lower) branch. Data was taken at $V_B = -820$ mV and $|\mathbf{B}| = 0.146$ T with orientation $\alpha = 30^\circ, \beta = 0^\circ$.

rotation (CROT)^{4,5,24,29,32–35} rely on the exchange interaction that arises from the wavefunction overlap between two adjacent QDs. For electrons in Si, two-qubit gate fidelities have recently surpassed 99% (refs. 30,31,34), but for holes in Si or FinFETs, the demonstration of two-qubit logic is still missing due to the challenges in obtaining a controllable exchange interaction³⁶.

We make an important step towards a FinFET-based quantum processor by demonstrating control over the exchange of two holes in a Si FinFET. While the exchange interaction is crucial for implementing high-fidelity two-qubit gates, it is, particularly for hole spins, still largely unexplored. We measure the dependence of the exchange splitting on the magnetic field direction and find large values in some directions but close-to-zero values in other directions. In addition, we develop a general theoretical framework applicable to a wide range of devices and identify the SOI as the main reason for the exchange anisotropy. From our measurements, we can extract the full exchange matrix and hence accurately determine the Hamiltonian of the two coupled spins, allowing us to predict the optimum operating points for the gates. For holes, unlike electrons, the strong exchange anisotropy facilitates CROTs with both high fidelity and high speed, for an experimental setting that is robust against device variations.

Figure 1a shows the device cross-section along the triangular-shaped fin, revealing ultrashort lengths, highly uniform profiles and perfect alignment of the gate electrodes^{19,20}; Fig. 1b presents a three-dimensional illustration of the device. The double quantum dot (DQD) hosting qubits Q1 and Q2 is formed beneath plunger gates P1 and P2, and the barrier gate B provides control over the interdot tunnel coupling t_c (ref. 22). The distance between the QDs was chosen to match the spin–orbit length^{20,22}. Taking advantage of the strong SOI, all-electrical spin control is implemented by electric-dipole spin resonance (EDSR)^{37,38}. For this purpose, fast voltage pulses and microwave (MW) bursts are applied to P1 and a spin-flip is detected in the form of an increased spin blockade leakage current. The device is tuned close to the (1,1)–(0,2) charge transition, where (n, m) denotes a state with n (m) excess holes on the left (right) QD. In Fig. 1c, the eigenenergies of the two-spin states ($|\uparrow\uparrow\rangle, |\uparrow\downarrow\rangle, |\downarrow\uparrow\rangle, |\downarrow\downarrow\rangle$) in the (1,1) and the singlet ground state S_{02} in the (0,2) charge region are plotted as a function of the detuning ϵ , which describes the energy difference between the (1,1) and (0,2) charge states. While spin-conserving

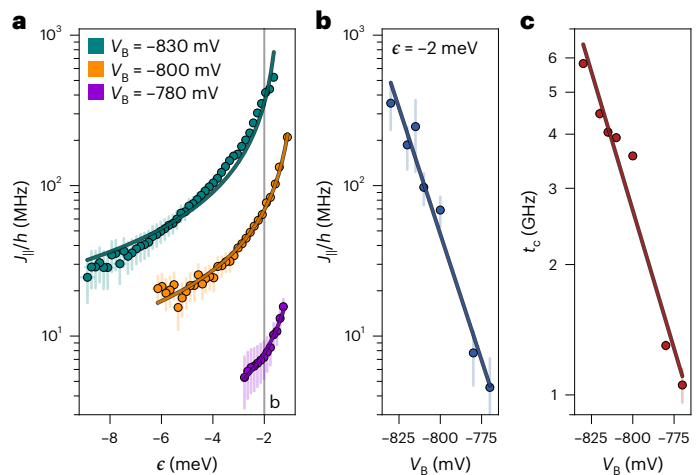


Fig. 2 | Tunable exchange coupling. a, Detuning dependence of the exchange frequency for $V_B = -830, -800$ and -780 mV. The solid curves represent fits to equation (1) and errors represent the width of the EDSR resonance. **b, c**, J_{\parallel}/h for $\epsilon = -2$ meV (**b**) and tunnel coupling (**c**) as functions of V_B , both determined from fits, as shown in **a**. The solid lines show exponential function fits to the data. The error bars in **b** represent the estimated errors due to a detuning uncertainty, and in **c** represent the standard errors for the best-fit values. Fitted U_0 values are provided in Supplementary Section 8.

tunnelling causes an anticrossing between the S_{02} and the antiparallel two-spin states, non-spin-conserving tunnelling due to the SOI results in an anticrossing between the S_{02} and the parallel two-spin states. As a consequence of the anticrossing with the singlet state, the energy of the antiparallel states decreases by $J_{\parallel}(\epsilon)/2$, where $J_{\parallel}(\epsilon)$ is the measured exchange splitting between the two spins. The energy-level structure of the two hole system can be probed by performing MW spectroscopy (Fig. 1d): at large negative ϵ , the resonance frequencies of both qubits differ due to the individual g -tensor \hat{g}_i for each QD and are independent of each other. At more positive detunings, closer to the (0,2) region, the exchange interaction splits both resonances by J_{\parallel}/h (h denotes Planck’s constant), resulting in four conditional transitions. The corresponding EDSR frequencies are denoted by $f_{i\sigma}$,

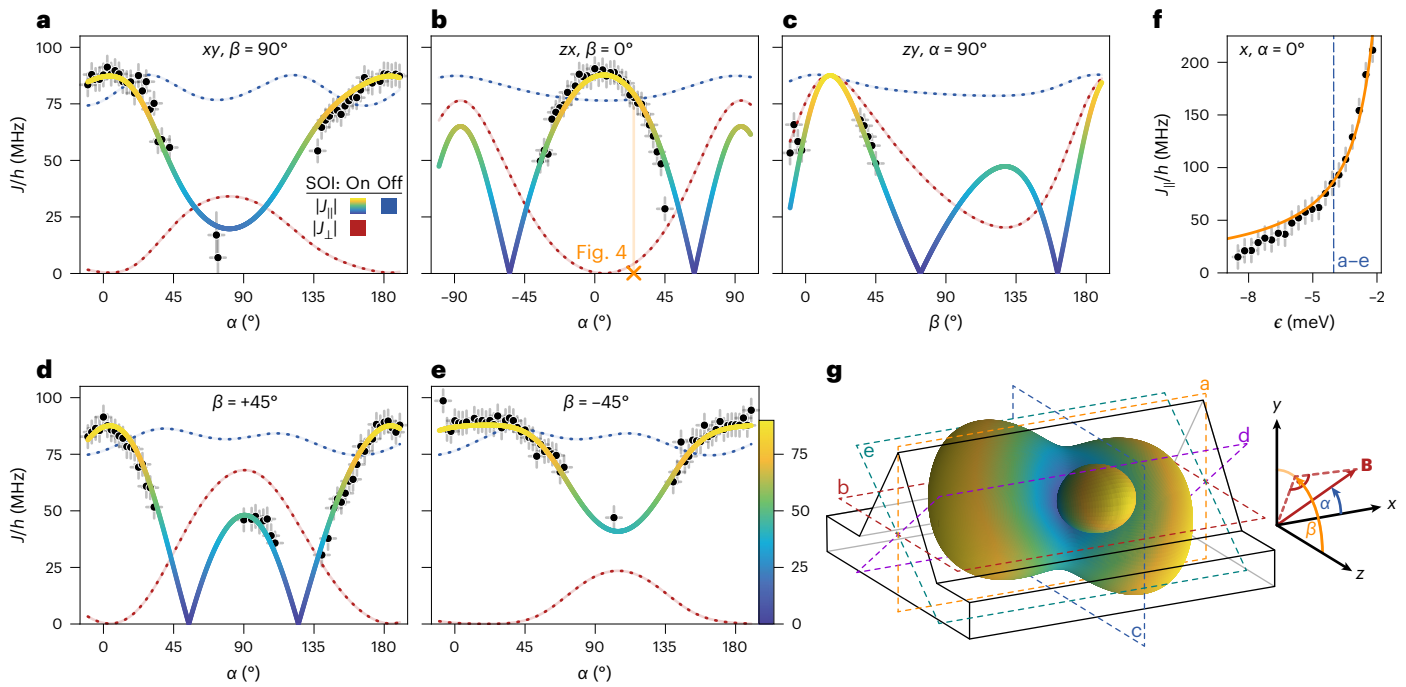


Fig. 3 | Anisotropic exchange. a–e, Exchange frequency as a function of magnetic field direction, which is expressed with the angles α and β (see coordinate system in **g**), for five different planes at $\epsilon = -4.03$ meV: α varies, $\beta = 90^\circ$ (**a**); α varies, $\beta = 0^\circ$ (**b**); $\alpha = 90^\circ$, β varies (**c**); α varies, $\beta = 45^\circ$ (**d**); and α varies, $\beta = -45^\circ$ (**e**). For certain B orientations, the qubits could not be read out via Pauli spin blockade and hence $J_{||}/h$ (black points) could not be determined. **f**, Detuning dependence of $J_{||}/h$ for B applied in the x direction. The multicoloured curves in **a–e** and the orange one in **f** represent a common fit of equation (3)

to all the data presented in this figure. While the red dashed curves in **a–e** visualize $|J_{\perp}|/h$, the blue dashed ones illustrate the exchange modulation due to the different and anisotropic g -tensors in the absence of SOI. **g**, Schematic representation of the fin structure (black and grey lines) overlaid by a 3D surface plot of $J_{||}/h$. The coloured dashed rectangles indicate the planes of **a–e**. The data presented in this figure are taken at $V_b = -820$ mV and the error bars account for the EDSR linewidth and uncertainties in B field due to magnetic flux trapping.

where i is the index of the target qubit and σ the control qubit state, $|\uparrow\rangle$ or $|\downarrow\rangle$.

We map out the ϵ -dependence of $J_{||}$ that, as shown in Fig. 2a, is well described by

$$J_{||} = J_0 \cos(2\tilde{\theta}) = \frac{2t_c^2}{U_0 - \epsilon} \cos(2\tilde{\theta}), \quad (1)$$

valid in the limit of $t_c \ll U_0 - \epsilon$ (refs. 39–41). Here, U_0 is an energy offset of the ϵ axis, J_0 the bare exchange and $\cos(2\tilde{\theta})$ an SOI-induced correction factor, which is discussed later. The exchange splitting shows an exponential dependence on the barrier gate voltage V_b (Fig. 2b) and reaches values of up to ~ 525 MHz. At the same time, exchange can be turned off within the resolution limit of our spectroscopy experiment that is given by the EDSR linewidth of ≈ 2 MHz (refs. 29, 33, 41). This means, using the two ‘control knobs’ ϵ and V_b , we achieve excellent control over the exchange coupling. As $t_c \propto J_{||}^{1/2}$, the tunnel coupling is also exponentially dependent on V_b and tunable by almost one order of magnitude (Fig. 2c).

In Fig. 3a–e, the dependence of $J_{||}$ on the magnetic field orientation is shown, revealing a striking anisotropy with vanishing splittings. The highly anisotropic exchange frequency is mainly due to the strong SOI and can be qualitatively understood from the gap size Δ_{so}^{dd} of the anticrossing between the S_{02} and the parallel two-spin states. Δ_{so}^{dd} is proportional to $|\hat{n}_{so} \times \mathbf{B}|$, where \mathbf{B} is the external magnetic field and \hat{n}_{so} a unit vector pointing in the direction of the spin–orbit field⁴². We expect $\hat{n}_{so} \propto \mathbf{k} \times \mathbf{E}$ with momentum operator \mathbf{k} and applied electric field \mathbf{E} (ref. 11). Therefore, Δ_{so}^{dd} changes with magnetic field orientation and so do the two hole energy levels (see Fig. 1c). However, we remark that from the dependence of Δ_{so}^{dd} on $\mathbf{B}/|\mathbf{B}|$, which is extracted close to zero detuning, the exchange matrix \hat{J} at the qubit operation

point cannot be extracted due to the voltage dependence of both the g -tensors and the SOI.

We derive an equation for \hat{J} starting from a Fermi–Hubbard model and including both the SOI and the anisotropic and differing hole g -tensors (Methods and Supplementary Section 5). Tuned deeply into the (1,1) charge regime where spin manipulation takes place, the system is approximated by the Hamiltonian

$$H_{(1,1)} = \frac{1}{2}\mu_B \mathbf{B} \cdot \hat{g}_1 \cdot \boldsymbol{\sigma}_1 + \frac{1}{2}\mu_B \mathbf{B} \cdot \hat{g}_2 \cdot \boldsymbol{\sigma}_2 + \frac{1}{4}\boldsymbol{\sigma}_1 \cdot \hat{J} \cdot \boldsymbol{\sigma}_2. \quad (2)$$

Here, μ_B is Bohr’s magneton and $\boldsymbol{\sigma}_i$ the vector of Pauli matrices for each QD. The exchange matrix is given by $\hat{J} = J_0 \hat{R}_{so}(-2d/\lambda_{so})$, where $\hat{R}_{so}(\varphi)$ is the counterclockwise rotation matrix around \hat{n}_{so} by an angle φ , λ_{so} is the spin–orbit length and d is the interdot distance. We use the convention that displacing a spin by $\pi\lambda_{so}/2$ induces a spin rotation of π (ref. 43). The experimentally observed exchange splitting is given by (Methods and Supplementary Section 5):

$$J_{||} = \hat{n}_1 \cdot \hat{J} \cdot \hat{n}_2 = J_0 \hat{n}_1 \cdot \hat{R}_{so}(-2d/\lambda_{so}) \cdot \hat{n}_2, \quad (3)$$

where $\hat{n}_i = \hat{g}_i \cdot \mathbf{B}/|\hat{g}_i \cdot \mathbf{B}|$ denotes the Zeeman field direction. On comparing equations (1) and (3), we find for the previously introduced correction factor $\cos(2\tilde{\theta}) = \hat{n}_1 \cdot \hat{R}_{so}(-2d/\lambda_{so}) \cdot \hat{n}_2$. Finally, by describing the magnetic field direction using the two angles α and β (Fig. 3), we obtain a fit equation $J_{||}(\alpha, \beta)$ with five fitting parameters, namely t_c , U_0 , \hat{n}_{so} and λ_{so} .

Next, we apply this model to the data (black points) shown in Fig. 3a–f and perform a common fit to the full data set, consisting of measurements of $J_{||}(\alpha, \beta)$ in five different planes (visualized in Fig. 3g) at constant detuning and for $J_{||}(\epsilon)$ for B pointing in the x direction. There

is excellent agreement between theory and experiment for the best-fit parameters: $\lambda_{\text{so}} = 31$ nm, $\hat{\mathbf{n}}_{\text{so}} = (-0.06, 0.41, 0.91)$, $t_c = 5.61$ GHz and $U_0 = 1.07$ meV. The spin-orbit length coincides with the values reported previously^{20,22} and corresponds to a spin rotation angle of $2\theta_{\text{so}} = 2d/\lambda_{\text{so}} \approx 0.82\pi$ for a hole tunnelling from one QD to the other over $d \approx 40$ nm. The direction of the spin-orbit field, represented by $(\alpha_{\text{so}} = 93^\circ, \beta_{\text{so}} = 23^\circ)$ is, as expected, perpendicular to the long axis of the fin and thus orthogonal to the hole momentum^{11,13}. The small out-of-the-substrate-plane tilt can arise on account of strain or electric fields not being perfectly aligned along the y direction. Using the five best-fit parameter values, we can reconstruct the full exchange matrix

$$\hat{J} = J_0 \begin{pmatrix} -0.87 & 0.41 & -0.28 \\ -0.49 & -0.60 & 0.64 \\ 0.10 & 0.69 & 0.72 \end{pmatrix}. \quad (4)$$

Because we also find the g -tensors when measuring $J_{\parallel}(\alpha, \beta)$ by means of MW spectroscopy, the two-spin Hamiltonian (equation (2)) is fully characterized, thus allowing us to optimize two-qubit gate operations, as discussed later. Furthermore, we can analyse the different contributions to the exchange anisotropy with equation (3): by setting θ_{so} to zero, we are left with the effect of the anisotropic g -tensors. We find that the g -tensor contribution to the J_{\perp} -anisotropy was minor (dashed blue curves in Fig. 3a–e). Finally, we remark that the observed rotational exchange anisotropy relies on a strong SOI and the presence of an external magnetic field^{44,45}, as opposed to a weaker Ising-like anisotropy that can be found in inversion symmetric hole DQDs⁴⁶ or at zero magnetic field^{147,48}.

We make use of the large exchange splitting to demonstrate a fast two-qubit CROT^{4,5,24,29,32–35} for holes in Si. This quantum operation is naturally implemented by driving just one of the four EDSR transitions (Fig. 1d), resulting in a rotation of the target qubit conditional on the state of the control qubit. First, we initialize $|\downarrow\downarrow\rangle$ in the $|\downarrow\uparrow\rangle$ -state by pulsing from $\epsilon > 0$, where the spin-blockaded $|\downarrow\downarrow\rangle$ -state is occupied, to $\epsilon = -2.9$ meV, where $J_{\parallel}/h \approx 80$ MHz and MW-induced state leakage is suppressed²⁹ (Supplementary Section 4). Subsequently, the state of the control qubit Q2 is prepared by a MW burst of length t_{b2} and frequency $f_{2\downarrow}$, and finally a CROT of the target qubit Q1 is triggered by the subsequent pulse with t_{b1} and $f_{1\uparrow}$ (Fig. 4a). The measurement outcome is presented in Fig. 4b, revealing the characteristic fading in and out of the target qubit's Rabi oscillations as a function of t_{b2} , that is, the spin state of the control qubit^{5,35}. A controlled spin-flip for Q1 is executed in ~ 24 ns, which is short compared to other realizations with electrons in Si (ref. 34) or holes in Ge (refs. 5,35). We remark that our transport-based readout scheme prevents single-shot spin measurements and severely limits the duration of the qubits' manipulation stage²², such that randomized benchmarking to determine a two-qubit gate fidelity could not be performed⁴⁹.

A conditional spin-flip provides a natural way of implementing a controlled-NOT (CNOT) gate, differing from a CROT only by a phase factor. Two key requirements need to be fulfilled for high-fidelity CROT gates. First, to prevent a mixing of the antiparallel spin states ($|\downarrow\downarrow\rangle, |\downarrow\uparrow\rangle$), the Zeeman energy difference between the qubits ΔE_z must be much larger than the 'perpendicular' exchange coupling $J_{\perp}(J_{\parallel}/J_{\perp})$ induces SWAP/controlled-phase oscillations^{29,30,40}. Second, either $J_{\parallel} \gg hf_{\text{Rabi}}$ or $J_{\parallel}/\sqrt{15} = hf_{\text{Rabi}}$ to avoid unwanted rotations of the off-resonant states^{34,40}. Hence, for electrons with isotropic exchange ($J_{\parallel} = J_{\perp} = J$) the speed of high-fidelity CROT gates is limited by $hf_{\text{Rabi}} \ll J \ll \Delta E_z$. However, for hole spins with highly anisotropic exchange interaction, this limit can be overcome. In fact, $J_{\parallel} = J_0$ while $J_{\perp} = 0$ is possible, for instance, if the g -tensors are isotropic, for $\theta_{\text{so}} = \pi/2$ and \mathbf{B} perpendicular to $\hat{\mathbf{n}}_{\text{so}}$ we remark that the latter condition also ensures fast single-qubit rotations. Consequently, our theory predicts that for holes in comparison to electrons, a CNOT gate with fidelity above 99% can be realized with

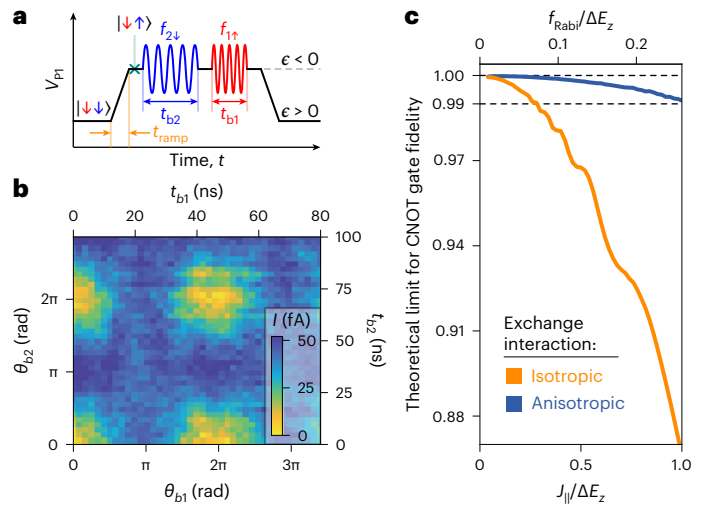


Fig. 4 | Fast two-qubit CROT for Si hole spin qubits. **a**, Pulse sequence for the CROT operation. A trapezoidal waveform with a ramp time of 20 ns is used to initialize the spins in the $|\downarrow\uparrow\rangle$ -state and to read out their state after applying two microwave bursts resonant with Q2 ($f_{2\downarrow} = 4.25$ GHz) and Q1 ($f_{1\uparrow} = 4.66$ GHz). **b**, Parity measurement of the qubits demonstrating a conditional rotation of Q1 controlled by the state of Q2. This data is taken at $J_{\parallel}/h \approx 80$ MHz, $V_B = -810$ mV, $|\mathbf{B}| = 0.146$ T, $\alpha = 25^\circ, \beta = 0^\circ$ and $\epsilon = -2.9$ meV. **c**, Numerically calculated CNOT gate fidelity versus exchange splitting J_{\parallel} (bottom x axis) and $f_{\text{Rabi}} = J_{\parallel}/\sqrt{15}/h$ (top x axis, both axes in units of ΔE_z) for anisotropic exchange, with parameters as in **b** (blue) and isotropic exchange (orange). The shaded regions indicate the precision of the numerics.

much shorter gate times (Fig. 4c). The gate fidelities presented in Fig. 4c were numerically calculated in the absence of incoherent noise, that is, the gate infidelities are due to Hamiltonian errors³¹ (Supplementary Section 7). For the controlled rotation operation presented in Fig. 4b the magnetic field orientation (marked by the vertical orange line in Fig. 3b) was chosen such that both a close-to-ideal exchange configuration ($|J_{\parallel}| = 0.90J_0, |J_{\perp}| = 0.05J_0$) and good readout contrast were achieved. In Fig. 3a–e the red dashed curves show the dependence of J_{\perp} on $\mathbf{B}/|\mathbf{B}|$, highlighting that the ideal configuration ($J_{\parallel} \approx J_0, J_{\perp} \approx 0$) is stretched over a wide range of directions. The CROT sweet spot is consequently tolerant to device variations, making this concept suitable for large qubit arrays, a point reinforced by the low variability and disorder resulting from industrial manufacturing^{21,50} and the electrical tunability of the SOI^{11,13}.

In summary, we investigated the exchange coupling between two hole-spins in a Si FinFET and found it to be both highly anisotropic and tunable, allowing for an interaction strength >0.5 GHz. We identify the strong SOI as the main microscopic origin of this anisotropy and propose a simple procedure for determining the exchange matrix. This measurement and analysis scheme applies to a wide variety of devices, for instance, to electron spin qubits with synthetic SOI in the presence of a magnetic field gradient (Supplementary Section 6)^{4,29,34}. By fully characterizing the Hamiltonian of the two coupled spins, the best possible configuration for implementing two-qubit gates can be identified. A strongly anisotropic exchange results in extended sweet spots in magnetic field orientation, where both fast and high-fidelity CROT gates can be performed. Finally, by choosing a close-to-ideal configuration we realize a controlled spin-flip in just ~ 24 ns.

Future improvements in device fabrication^{21,50}, assisted by high-volume characterization^{51,52}, are needed to reduce device variability. Low-variability devices, combined with robust CROT sweet spots, will make two-qubit gate operations with anisotropic exchange highly attractive for large-scale qubit arrays. The concepts presented here are, in principle, compatible with elevated temperatures, but experimental confirmation is presently lacking. The advances reported

here, if they can be combined with fast readout⁵³ and operation above 1 K, would show that industrial FinFET technology has great potential for realizing a universal quantum processor, integrated on the same chip with the classical control electronics.

Online content

Any methods, additional references, Nature Portfolio reporting summaries, source data, extended data, supplementary information, acknowledgements, peer review information; details of author contributions and competing interests; and statements of data and code availability are available at <https://doi.org/10.1038/s41567-024-02481-5>.

References

1. Loss, D. & DiVincenzo, D. P. Quantum computation with quantum dots. *Phys. Rev. A* **57**, 120–126 (1998).
2. Vandersypen, L. M. K. et al. Interfacing spin qubits in quantum dots and donors—hot, dense, and coherent. *npj Quantum Inf* **3**, 34 (2017).
3. Veldhorst, M., Eenink, H. G. J., Yang, C. H. & Dzurak, A. S. Silicon CMOS architecture for a spin-based quantum computer. *Nat. Commun.* **8**, 1766 (2017).
4. Philips, S. G. J. et al. Universal control of a six-qubit quantum processor in silicon. *Nature* **609**, 919–924 (2022).
5. Hendrickx, N. W. et al. A four-qubit germanium quantum processor. *Nature* **591**, 580–585 (2021).
6. Tokura, Y., van der Wiel, W. G., Obata, T. & Tarucha, S. Coherent single electron spin control in a slanting Zeeman field. *Phys. Rev. Lett.* **96**, 047202 (2006).
7. Pioro-Ladrière, M. et al. Electrically driven single-electron spin resonance in a slanting Zeeman field. *Nat. Phys.* **4**, 776–779 (2008).
8. Gilbert, W. et al. On-demand electrical control of spin qubits. *Nat. Nanotechnol.* **18**, 131–136 (2023).
9. Prechtel, J. H. et al. Decoupling a hole spin qubit from the nuclear spins. *Nat. Mater.* **15**, 981–986 (2016).
10. Zwanenburg, F. A. et al. Silicon quantum electronics. *Rev. Mod. Phys.* **85**, 961 (2013).
11. Kloeffel, C., Rančić, M. J. & Loss, D. Direct Rashba spin-orbit interaction in Si and Ge nanowires with different growth directions. *Phys. Rev. B* **97**, 235422 (2018).
12. Bosco, S. & Loss, D. Fully tunable hyperfine interactions of hole spin qubits in Si and Ge quantum dots. *Phys. Rev. Lett.* **127**, 190501 (2021).
13. Bosco, S., Hetényi, B. & Loss, D. Hole spin qubits in Si FinFETs with fully tunable spin-orbit coupling and sweet spots for charge noise. *PRX Quantum* **2**, 010348 (2021).
14. Froning, F. N. M. et al. Ultrafast hole spin qubit with gate-tunable spin-orbit switch functionality. *Nat. Nanotechnol.* **16**, 308–312 (2021).
15. Wang, K. et al. Ultrafast coherent control of a hole spin qubit in a germanium quantum dot. *Nat. Commun.* **13**, 206 (2022).
16. Piot, N. et al. A single hole spin with enhanced coherence in natural silicon. *Nat. Nanotechnol.* **17**, 1072–1077 (2022).
17. Auth, C. et al. A 22nm high performance and low-power CMOS technology featuring fully-depleted tri-gate transistors, self-aligned contacts and high density MIM capacitors. In *2012 Symposium on VLSI Technology (VLSIT)* 131–132 (IEEE, 2012).
18. Maurand, R. et al. A CMOS silicon spin qubit. *Nat. Commun.* **7**, 13575 (2016).
19. Kuhlmann, A. V., Deshpande, V., Camenzind, L. C., Zumbühl, D. M. & Fuhrer, A. Ambipolar quantum dots in undoped silicon fin field-effect transistors. *Appl. Phys. Lett.* **113**, 122107 (2018).
20. Geyer, S. et al. Self-aligned gates for scalable silicon quantum computing. *Appl. Phys. Lett.* **118**, 104004 (2021).
21. Zwerver, A. M. J. et al. Qubits made by advanced semiconductor manufacturing. *Nat. Electron.* **5**, 184–190 (2022).
22. Camenzind, L. C. et al. A hole spin qubit in a fin field-effect transistor above 4 kelvin. *Nat. Electron.* **5**, 178–183 (2022).
23. Gonzalez-Zalba, M. F. et al. Scaling silicon-based quantum computing using CMOS technology. *Nat. Electron.* **4**, 872–884 (2021).
24. Petit, L. et al. Universal quantum logic in hot silicon qubits. *Nature* **580**, 355–359 (2020).
25. Yang, C. H. et al. Operation of a silicon quantum processor unit cell above one kelvin. *Nature* **580**, 350–354 (2020).
26. Xue, X. et al. CMOS-based cryogenic control of silicon quantum circuits. *Nature* **593**, 205–210 (2021).
27. Petta, J. R. et al. Coherent manipulation of coupled electron spins in semiconductor quantum dots. *Science* **309**, 2180–2184 (2005).
28. Veldhorst, M. et al. A two-qubit logic gate in silicon. *Nature* **526**, 410–414 (2015).
29. Watson, T. F. et al. A programmable two-qubit quantum processor in silicon. *Nature* **555**, 633–637 (2018).
30. Mills, A. R. et al. Two-qubit silicon quantum processor with operation fidelity exceeding 99%. *Sci. Adv.* **8**, 14 (2022).
31. Xue, X. et al. Quantum logic with spin qubits crossing the surface code threshold. *Nature* **601**, 343–347 (2022).
32. Zajac, D. M. et al. Resonantly driven CNOT gate for electron spins. *Science* **359**, 439–442 (2018).
33. Huang, W. et al. Fidelity benchmarks for two-qubit gates in silicon. *Nature* **569**, 532–536 (2019).
34. Noiri, A. et al. Fast universal quantum gate above the fault-tolerance threshold in silicon. *Nature* **601**, 338–342 (2022).
35. Hendrickx, N. W. et al. A single-hole spin qubit. *Nat. Commun.* **11**, 3478 (2020).
36. Fang, Y., Philippopoulos, P., Culcer, D., Coish, W. A. & Chesi, S. Recent advances in hole-spin qubits. *Mater. Quantum Technol.* **3**, 012003 (2023).
37. Golovach, V. N., Borhani, M. & Loss, D. Electric-dipole-induced spin resonance in quantum dots. *Phys. Rev. B* **74**, 165319 (2006).
38. Nowack, K. C., Koppens, F. H. L., Nazarov, Y. V. & Vandersypen, L. M. K. Coherent control of a single electron spin with electric fields. *Science* **318**, 1430–1433 (2007).
39. Stepanenko, D., Rudner, M., Halperin, B. I. & Loss, D. Singlet-triplet splitting in double quantum dots due to spin-orbit and hyperfine interactions. *Phys. Rev. B* **85**, 075416 (2012).
40. Russ, M. et al. High-fidelity quantum gates in Si/SiGe double quantum dots. *Phys. Rev. B* **97**, 085421 (2018).
41. Hendrickx, N. W., Franke, D. P., Sammak, A., Scappucci, G. & Veldhorst, M. Fast two-qubit logic with holes in germanium. *Nature* **577**, 487–491 (2020).
42. Nadj-Perge, S. et al. Spectroscopy of spin-orbit quantum bits in indium antimonide nanowires. *Phys. Rev. Lett.* **108**, 166801 (2012).
43. Froning, F. N. M. et al. Strong spin-orbit interaction and *g*-factor renormalization of hole spins in Ge/Si nanowire quantum dots. *Phys. Rev. Res.* **3**, 013081 (2021).
44. Kavokin, K. V. Anisotropic exchange interaction of localized conduction-band electrons in semiconductors. *Phys. Rev. B* **64**, 075305 (2001).
45. Kavokin, K. V. Symmetry of anisotropic exchange interactions in semiconductor nanostructures. *Phys. Rev. B* **69**, 075302 (2004).
46. Hetényi, B., Kloeffel, C. & Loss, D. Exchange interaction of hole-spin qubits in double quantum dots in highly anisotropic semiconductors. *Phys. Rev. Res.* **2**, 033036 (2020).
47. Hetényi, B., Bosco, S. & Loss, D. Anomalous zero-field splitting for hole spin qubits in Si and Ge quantum dots. *Phys. Rev. Lett.* **129**, 116805 (2022).
48. Katsaros, G. et al. Zero field splitting of heavy-hole states in quantum dots. *Nano Lett.* **20**, 5201–5206 (2020).
49. Knill, E. et al. Randomized benchmarking of quantum gates. *Phys. Rev. A* **77**, 012307 (2008).

50. Elsayed, A. et al. Low charge noise quantum dots with industrial CMOS manufacturing. Preprint at <https://doi.org/10.48550/arXiv.2212.06464> (2022).
51. de Kruijf, M. et al. A compact and versatile cryogenic probe station for quantum device testing. *Rev. Sci. Instrum.* **94**, 054707, <https://doi.org/10.1063/5.0139825> (2023).
52. Neyens, S. et al. Probing single electrons across 300 mm spin qubit wafers. Preprint at <https://doi.org/10.48550/arXiv.2307.04812> (2023).
53. Huang, J. Y. et al. A high-sensitivity charge sensor for silicon qubits above 1 K. *Nano Lett.* **21**, 6328–6335 (2021).

Publisher's note Springer Nature remains neutral with regard to jurisdictional claims in published maps and institutional affiliations.

Open Access This article is licensed under a Creative Commons Attribution 4.0 International License, which permits use, sharing, adaptation, distribution and reproduction in any medium or format, as long as you give appropriate credit to the original author(s) and the source, provide a link to the Creative Commons licence, and indicate if changes were made. The images or other third party material in this article are included in the article's Creative Commons licence, unless indicated otherwise in a credit line to the material. If material is not included in the article's Creative Commons licence and your intended use is not permitted by statutory regulation or exceeds the permitted use, you will need to obtain permission directly from the copyright holder. To view a copy of this licence, visit <http://creativecommons.org/licenses/by/4.0/>.

© The Author(s) 2024

Methods

Device fabrication

The fin structures are orientated along the [110] crystal direction on a near-intrinsic, natural Si substrate ($\rho > 10$ k Ω cm and (100) surface) and are covered by an ≈ 7 -nm-thick, thermally grown silicon dioxide (SiO₂) layer. Two layers of titanium nitride gate electrodes, which are electrically isolated by a ≈ 4.5 -nm-thick SiO₂ layer deposited by atomic layer deposition, are used for DQD formation. The second gate layer is integrated by a self-aligned process, resulting in a perfect layer-to-layer alignment. The p-type source and drain regions are made of platinum silicide. Finally, the devices are embedded in an ≈ 100 -nm-thick SiO₂ layer and are measured through contact vias filled with tungsten. Further details on the device fabrication are provided in refs. 19,20.

Experimental setup

All measurements are performed using a Bluefors dry dilution refrigerator with a base temperature of ~ 40 mK and a three-axis magnet that provides arbitrary control of the magnetic field vector \mathbf{B} . The d.c. voltages are supplied by a low-noise voltage source (BasPI SP927) and the fast pulses applied to the P1-gate (Fig. 1a) by an arbitrary waveform generator (Tektronix AWG5208), which also controls the I and Q inputs of a vector signal generator (Rohde & Schwarz SGS100A) for generating sideband-modulated EDSR microwave pulses. The source-to-drain current is measured with a current-to-voltage amplifier (BasPI SP983c) and a lock-in amplifier (Signal Recovery 7265), chopping the microwave signal at a frequency of 89.2 Hz for better noise rejection. Further details are provided in Supplementary Section 1.

Derivation of the fit function for the exchange matrix

Using a Fermi–Hubbard model with a single orbital state $|i\rangle$ per site $i = \{1, 2\}$, our DQD system is described by the Hamiltonian

$$H_{\text{FH}} = \sum_{i,j \in \{1,2\}} \sum_{s,s' \in \{\uparrow,\downarrow\}} \tilde{H}_{ij}^{ss'} a_{js'}^\dagger a_{is} + U \sum_{i \in \{1,2\}} n_{i\uparrow} n_{i\downarrow}. \quad (5)$$

Here a_{is}^\dagger (a_{is}) creates (removes) a hole on site i and spin $s = \{\uparrow, \downarrow\}$, $n_{is} = a_{is}^\dagger a_{is}$ is the occupation number operator, and U is the charging energy. The single-particle Hamiltonian \tilde{H} is given by

$$\tilde{H} = \frac{\tilde{\epsilon}}{2} \tau_z + t_c \cos(\theta_{\text{so}}) \tau_x + t_c \sin(\theta_{\text{so}}) \tau_y \hat{\mathbf{n}}_{\text{so}} \cdot \boldsymbol{\sigma} + \frac{1}{2} \mu_B \mathbf{B} \cdot \left[\frac{1+\tau_z}{2} \hat{\mathbf{g}}_1 \cdot \boldsymbol{\sigma} + \frac{1-\tau_z}{2} \hat{\mathbf{g}}_2 \cdot \boldsymbol{\sigma} \right], \quad (6)$$

and contains spin-conserving interdot tunnelling $t_c \cos(\theta_{\text{so}}) \tau_x$ and an SOI-induced spin-flip hopping term $t_c \sin(\theta_{\text{so}}) \tau_y \hat{\mathbf{n}}_{\text{so}} \cdot \boldsymbol{\sigma}$. Here we use the convention that the gap size of the anticrossing of two tunnel-coupled states is given by $2\sqrt{2}t_c$. Moreover, (τ_x, τ_y, τ_z) are the Pauli matrices for the orbital degree of freedom, for example $\tau_z = |1\rangle\langle 1| - |2\rangle\langle 2|$, and $\boldsymbol{\sigma}$ is the vector of Pauli matrices acting on the spin degree of freedom. In the laboratory frame, as defined in Fig. 1, the $\hat{\mathbf{g}}$ -tensors $\hat{\mathbf{g}}_1$ and $\hat{\mathbf{g}}_2$ are symmetric (Supplementary Section 3). Finally, $\tilde{\epsilon}$ is the energy difference for a hole occupying the left or the right QD and is expressed in terms of the detuning energy ϵ between the (1,1) and (0,2) charge states by $\tilde{\epsilon} = \epsilon + U - U_0$.

We perform a transformation from the laboratory frame to the so-called ‘spin–orbit frame’ and find

$$\tilde{H}^{\text{so}} = U_{\text{so}}^\dagger \tilde{H} U_{\text{so}} = \frac{\tilde{\epsilon}}{2} \tau_z + t_c \tau_x + \frac{1}{2} \mu_B \mathbf{B} \cdot \left[\frac{1+\tau_z}{2} \hat{\mathbf{g}}_1^{\text{so}} \cdot \boldsymbol{\sigma} + \frac{1-\tau_z}{2} \hat{\mathbf{g}}_2^{\text{so}} \cdot \boldsymbol{\sigma} \right]. \quad (7)$$

In the spin–orbit frame, non-spin-conserving tunnelling is gauged away by the unitary transformation $U_{\text{so}} = \exp(-i\theta_{\text{so}} \tau_z \hat{\mathbf{n}}_{\text{so}} \cdot \boldsymbol{\sigma}/2)$, and the $\hat{\mathbf{g}}$ -tensors are given by $\hat{\mathbf{g}}_1^{\text{so}} = \hat{\mathbf{g}}_1 \cdot \hat{R}_{\text{so}}(\theta_{\text{so}})$ and $\hat{\mathbf{g}}_2^{\text{so}} = \hat{\mathbf{g}}_2 \cdot \hat{R}_{\text{so}}(-\theta_{\text{so}})$. Here $\hat{R}_{\text{so}}(\varphi)$ denotes a counterclockwise rotation around $\hat{\mathbf{n}}_{\text{so}}$ by an angle φ .

As our DQD system is operated close to the $|S_{02}\rangle$ - $|S\rangle$ anticrossing, the Hamiltonian H_{FH} can be represented in the basis $\{|S_{02}\rangle, |S\rangle, |T_-\rangle, |T_+\rangle, |T_0\rangle\}$

$$H_{5 \times 5} = \begin{pmatrix} U_0 - \epsilon & \sqrt{2}t_c & 0 & 0 & 0 \\ \sqrt{2}t_c & 0 & -\frac{\delta b_x + i\delta b_y}{\sqrt{2}} & \frac{\delta b_x - i\delta b_y}{\sqrt{2}} & \delta b_z \\ 0 & -\frac{\delta b_x - i\delta b_y}{\sqrt{2}} & \bar{b}_z & 0 & \frac{b_x - ib_y}{\sqrt{2}} \\ 0 & \frac{\delta b_x + i\delta b_y}{\sqrt{2}} & 0 & -\bar{b}_z & \frac{b_x + ib_y}{\sqrt{2}} \\ 0 & \delta b_z & \frac{b_x + ib_y}{\sqrt{2}} & \frac{b_x - ib_y}{\sqrt{2}} & 0 \end{pmatrix}, \quad (8)$$

where the average and gradient Zeeman fields $\bar{b} = \mu_B \mathbf{B} \cdot (\hat{\mathbf{g}}_1^{\text{so}} + \hat{\mathbf{g}}_2^{\text{so}})/2$ and $\delta b = \mu_B \mathbf{B} \cdot (\hat{\mathbf{g}}_1^{\text{so}} - \hat{\mathbf{g}}_2^{\text{so}})/2$ were introduced. In the spin–orbit frame, the singlet subspace $\{|S_{02}\rangle, |S\rangle\}$ is coupled by the total tunnel coupling t_c and the hybridized singlets S_\pm have energies $E_{S_\pm} = U_0 - \epsilon + J_0$ and $E_{S_-} = -J_0$ with $J_0 = \sqrt{2} \tan(\gamma/2) = -(U_0 - \epsilon)[1 - \sqrt{1 + 8t_c^2/(U_0 - \epsilon)^2}]/2$ and mixing angle $\gamma = \arctan[\sqrt{8}t_c/(U_0 - \epsilon)]$. Furthermore, we remark that $J_0 \approx 2t_c^2/(U_0 - \epsilon)$ in the limit of $t_c/(U_0 - \epsilon) \ll 1$. Because S_\pm couples only weakly to the triplet states, our Hilbert space can be restricted to the four levels $\{|S_-\rangle, |T_-\rangle, |T_+\rangle, |T_0\rangle\}$ and we obtain

$$H_{4 \times 4} = \begin{pmatrix} -J_0 & -\frac{\delta b_x + i\delta b_y}{\sqrt{2}} \cos(\frac{\gamma}{2}) & \frac{\delta b_x - i\delta b_y}{\sqrt{2}} \cos(\frac{\gamma}{2}) & \delta b_z \cos(\frac{\gamma}{2}) \\ -\frac{\delta b_x - i\delta b_y}{\sqrt{2}} \cos(\frac{\gamma}{2}) & \bar{b}_z & 0 & \frac{b_x - ib_y}{\sqrt{2}} \\ \frac{\delta b_x + i\delta b_y}{\sqrt{2}} \cos(\frac{\gamma}{2}) & 0 & -\bar{b}_z & \frac{b_x + ib_y}{\sqrt{2}} \\ \delta b_z \cos(\frac{\gamma}{2}) & \frac{b_x + ib_y}{\sqrt{2}} & \frac{b_x - ib_y}{\sqrt{2}} & 0 \end{pmatrix}. \quad (9)$$

Hole spin manipulation is performed deep in the (1,1) charge stability region, allowing us to introduce the localized spin operators $\boldsymbol{\sigma}_1^{\text{so}}$ and $\boldsymbol{\sigma}_2^{\text{so}}$. The Hamiltonian (9) can then be written as

$$H_{(1,1)}^{\text{so}} = \frac{1}{2} \mu_B \mathbf{B} \cdot \hat{\mathbf{g}}_1^{\text{so}} \cdot \boldsymbol{\sigma}_1^{\text{so}} + \frac{1}{2} \mu_B \mathbf{B} \cdot \hat{\mathbf{g}}_2^{\text{so}} \cdot \boldsymbol{\sigma}_2^{\text{so}} + \frac{1}{4} J_0 \boldsymbol{\sigma}_1^{\text{so}} \cdot \boldsymbol{\sigma}_2^{\text{so}}, \quad (10)$$

revealing that the exchange interaction is isotropic in the spin–orbit frame. To find an expression for the experimentally measured values, we first rewrite equation (10) in the lab frame:

$$H_{(1,1)}^{\text{lab}} = \frac{1}{2} \mu_B \mathbf{B} \cdot \hat{\mathbf{g}}_1 \cdot \boldsymbol{\sigma}_1 + \frac{1}{2} \mu_B \mathbf{B} \cdot \hat{\mathbf{g}}_2 \cdot \boldsymbol{\sigma}_2 + \frac{1}{4} \boldsymbol{\sigma}_1 \cdot \hat{\mathcal{J}} \cdot \boldsymbol{\sigma}_2. \quad (11)$$

Here $\hat{\mathcal{J}} = J_0 \hat{R}_{\text{so}}(-2\theta_{\text{so}})$ represents the exchange matrix in the lab frame, $\boldsymbol{\sigma}_1 = \hat{R}_{\text{so}}(-\theta_{\text{so}}) \cdot \boldsymbol{\sigma}_1^{\text{so}}$ and $\boldsymbol{\sigma}_2 = \hat{R}_{\text{so}}(\theta_{\text{so}}) \cdot \boldsymbol{\sigma}_2^{\text{so}}$. In addition, independent rotations \hat{R}_1 and \hat{R}_2 are applied to Q1 and Q2, such that the single-particle terms of the Hamiltonian (11) become diagonal:

$$H_{(1,1)}^{\text{Q}} = \frac{1}{2} E_{Z,1} \sigma_{z,1}^{\text{Q}} + \frac{1}{2} E_{Z,2} \sigma_{z,2}^{\text{Q}} + \frac{1}{4} \boldsymbol{\sigma}_1^{\text{Q}} \cdot \hat{\mathcal{J}}^{\text{Q}} \cdot \boldsymbol{\sigma}_2^{\text{Q}}, \quad (12)$$

where $E_{Z,i} \mathbf{e}_z^{\text{Q}} = \mu_B \hat{R}_i \cdot \hat{\mathbf{g}}_i \cdot \mathbf{B}$ is the i -th site’s Zeeman splitting, \mathbf{e}_z^{Q} the spin quantization axis and $\hat{\mathcal{J}}^{\text{Q}} = J_0 \hat{R}_1 \cdot \hat{R}_{\text{so}}(-2\theta_{\text{so}}) \cdot \hat{R}_2^T$ the exchange matrix in the so-called ‘qubit frame’, wherein the exchange splitting J_{\parallel} is experimentally observed. To obtain an expression for J_{\parallel} we rewrite the Hamiltonian of equation (12) in matrix form using the two-qubit basis $\{|\uparrow\uparrow\rangle, |\uparrow\downarrow\rangle, |\downarrow\uparrow\rangle, |\downarrow\downarrow\rangle\}$

$$H_{(1,1)}^{\text{Q}} = \begin{pmatrix} E_Z + \frac{1}{4} J_{ZZ}^{\text{Q}} & 0 & 0 & 0 \\ 0 & \frac{1}{2} \Delta E_Z - \frac{1}{4} J_{ZZ}^{\text{Q}} & \frac{1}{2} J_{\perp} & 0 \\ 0 & \frac{1}{2} (J_{\perp})^* & -\frac{1}{2} \Delta E_Z - \frac{1}{4} J_{ZZ}^{\text{Q}} & 0 \\ 0 & 0 & 0 & -E_Z + \frac{1}{4} J_{ZZ}^{\text{Q}} \end{pmatrix}. \quad (13)$$

Here we neglect every coupling that would contribute to the eigenvalues in $\mathcal{O}(J_0^2/E_Z)$ and introduce $J_{\perp} = [J_{xx}^Q + J_{yy}^Q + i(J_{xy}^Q - J_{yx}^Q)]/2$, $E_Z = (E_{Z,1} + E_{Z,2})/2$ and $\Delta E_Z = E_{Z,1} - E_{Z,2}$. The eigenenergies of equation (13) are

$$E_{\uparrow\uparrow} = E_Z + \frac{1}{4}J_{zz}^Q, \quad E_{\downarrow\downarrow} = -E_Z + \frac{1}{4}J_{zz}^Q, \quad (14a)$$

$$E_{\uparrow\downarrow} = \frac{1}{2}\Delta E_Z - \frac{1}{4}J_{zz}^Q, \quad E_{\downarrow\uparrow} = -\frac{1}{2}\Delta E_Z - \frac{1}{4}J_{zz}^Q, \quad (14b)$$

with $\Delta E_Z = \sqrt{\Delta E_Z^2 + |J_{\perp}|^2}$. We thus find for the exchange splitting, which is defined as the energy difference between the two transitions flipping the same spin, $J_{\parallel} = E_{\uparrow\uparrow} - E_{\downarrow\downarrow} - (E_{\uparrow\downarrow} - E_{\downarrow\uparrow}) = J_{zz}^Q$. The matrix element J_{zz}^Q is in turn given by

$$J_{zz}^Q = J_{\parallel} = \mathbf{e}_z^Q \cdot \hat{g} \cdot \mathbf{e}_z^Q = \hat{\mathbf{n}}_1 \cdot \hat{g} \cdot \hat{\mathbf{n}}_2 = J_0 \hat{\mathbf{n}}_1 \cdot \hat{R}_{\text{so}}(-2\theta_{\text{so}}) \cdot \hat{\mathbf{n}}_2. \quad (15)$$

equation (15) is the fit function employed to describe the observed exchange anisotropy, where the effect of both SOI and the anisotropy of the g -tensors is accounted for. We note that an explicit dependence on the magnetic field direction arises from $\hat{\mathbf{n}}_i = \hat{g}_i \cdot \mathbf{B} / |\hat{g}_i \cdot \mathbf{B}|$. Further details of the derivation are found in Supplementary Section 5.

Numerical calculation of the CNOT gate fidelity

The CROT gate operation is modelled by numerically evaluating the Hamiltonian's time evolution

$$\text{CROT}_{\text{num}} = \mathcal{T} \exp \left[-\frac{i}{\hbar} \int_0^{t_{\pi}} H_{(1,1)}^Q(t) dt \right]. \quad (16)$$

Here \mathcal{T} denotes time-ordering, t_{π} is the spin-flip time, and the time-dependent Hamiltonian $H_{(1,1)}^Q(t)$ results from equation (13) after adding the drive $hf_{\text{Rabi}}^c \sin(2\pi f_{1\uparrow} t) \sigma_{x,1}$, where the Rabi frequency fulfils the condition $hf_{\text{Rabi}} = J_{\parallel}/\sqrt{15}$ to suppress off-resonant driving^{34,40}. Finally, the CNOT gate fidelity is determined by $\mathcal{F} = \frac{1}{4} |\text{Tr} [\text{CNOT}_{\text{num}} \text{CNOT}^{\dagger}]|$ where CNOT is the ideal gate matrix and CNOT_{num} is obtained by applying single-qubit phase corrections to equation (16). For more details, see Supplementary Section 7.

Data availability

The data supporting the plots within this paper are available via Zenodo at <https://doi.org/10.5281/zenodo.7547764> (ref. 54). Source data are provided with this paper.

References

54. Geyer, S. & Kuhlmann, A. Supporting Data for "Anisotropic exchange interaction of two hole spin qubits". Zenodo <https://doi.org/10.5281/zenodo.7547764> (2024).

Acknowledgements

We acknowledge the support of the cleanroom operation team, particularly U. Drechsler, A. Olziersky and D. D. Pineda, at the IBM Binnig and Rohrer Nanotechnology Center, and technical support at the University of Basel by S. Martin and M. Steinacher. In addition, we thank T. Berger for providing us with a 3D render of the FinFET device. This work was partially supported by the NCCR SPIN, the Swiss NSF (grant no. 179024) and the EU H2020 European Microkelvin Platform EMP (grant no. 824109). L.C.C. acknowledges support by a Swiss NSF mobility fellowship (P2BSP2_200127).

Author contributions

S.G. and A.V.K. conceived and performed the experiments, with inputs from L.C.C., R.E., R.J.W., A.F. and D.M.Z. A.V.K. and S.G. designed and fabricated the device, with support by A.F. B.H., S.B. and D.L. developed the theory model. S.G., A.V.K., B.H. and S.B. analysed the data and wrote the manuscript, with inputs from all the authors. A.V.K. managed the project with support from R.J.W. and D.M.Z.

Funding

Open access funding provided by University of Basel.

Competing interests

The authors declare no competing interests.

Additional information

Supplementary information The online version contains supplementary material available at <https://doi.org/10.1038/s41567-024-02481-5>.

Correspondence and requests for materials should be addressed to Simon Geyer, Dominik M. Zumbühl or Andreas V. Kuhlmann.

Peer review information *Nature Physics* thanks Andre Saraiva and the other, anonymous, reviewer(s) for their contribution to the peer review of this work.

Reprints and permissions information is available at www.nature.com/reprints.